PNAS RESEARCH ARTICLE | EARTH, ATMOSPHERIC, AND PLANETARY SCIENCES

The Greenland spatial fingerprint of Dansgaard–Oeschger events in observations and models

Christo Buizert[a,1], Todd A. Sowers[b], Kyle Niezgoda[a,c], Thomas Blunier[d], Vasileios Gkinis[d], Margaret Harlan[d,e], Chengfei He[f], Tyler R. Jones[g], Helle A. Kjaer[d], Jesper B. Liisberg[d], James A. Menking[a,h,i], Valerie Morris[g], David Noone[a,j], Sune Olander Rasmussen[d], Louise C. Sime[k], Jørgen P. Steffensen[d], Anders Svensson[d], Bruce H. Vaughn[g], Bo M. Vinther[d], and James W.C. White[g,l]

Affiliations are included on p. 8.

Edited by Mark Thiemens, University of California San Diego, La Jolla, CA; received February 6, 2024; accepted September 4, 2024

Pleistocene Ice Ages display abrupt Dansgaard–Oeschger (DO) climate oscillations that provide prime examples of Earth System tipping points—abrupt transition that may result in irreversible change. Greenland ice cores provide key records of DO climate variability, but gas-calibrated estimates of the temperature change magnitudes have been limited to central and northwest Greenland. Here, we present ice-core $\delta^{15}N\text{-}N_2$ records from south (Dye 3) and coastal east Greenland (Renland) to calibrate the local water isotope thermometer and provide a Greenland-wide spatial characterization of DO event magnitude. We combine these data with existing records of $\delta^{18}O$, deuterium excess, and accumulation rates to create a multiproxy "fingerprint" of the DO impact on Greenland. Isotope-enabled climate models have skill in simulating the observational multiproxy DO event impact, and we use a series of idealized simulations with such models to identify regions of the North Atlantic that are critical in explaining DO variability. Our experiments imply that wintertime sea ice variation in the subpolar gyre, rather than the commonly invoked Nordic Seas, is both a sufficient and a necessary condition to explain the observed DO impacts in Greenland, whatever the distal cause. Moisture-tagging experiments support the idea that Greenland DO isotope signals may be explained almost entirely via changes in the vapor source distribution and that site temperature is not a main control on $\delta^{18}O$ during DO transitions, contrary to the traditional interpretation. Our results provide a comprehensive, multiproxy, data-model synthesis of abrupt DO climate variability in Greenland.

paleoclimate | ice cores | Greenland | Dansgaard–Oeschger cycle | water isotopes

Significance

Reconstructions of Earth's past climate show evidence for instability and abrupt change, which are of great scientific and societal importance. The Dansgaard–Oeschger (DO) oscillation of the last Ice Age, which is most clearly observed in Greenland ice cores, is the prime example of such instability. Here, we provide new ice-core observations from southern and coastal eastern Greenland and combine these with existing data to create a Greenland-wide, multiparameter assessment of the climate impact of DO events. State-of-the-art climate model simulations of these events provide good agreement with the data. To explain the observations, models require winter sea ice in the North Atlantic to extend as far south as 45°N during the cold phases of the oscillation.

Reconstructions of Earth's past climatic and environmental conditions show evidence for the existence of tipping points: thresholds beyond which abrupt and often irreversible changes are initiated. Such tipping-point behavior—commonly associated with bistability, hysteresis, and the operation of strong positive climate feedbacks—has been suggested for Earth System components ranging from ice-sheet volume (1) to northern African hydroclimate (2). Understanding these dynamical systems in detail is of obvious scientific and societal importance, particularly in the face of ongoing anthropogenic climate change (3).

The prime example of tipping-point behavior is the Dansgaard–Oeschger (DO) cycle that occurred during Pleistocene Ice Ages (4, 5). The DO cycle consists of a millennial-scale alternating sequence of North Atlantic cold (stadial) and warm (interstadial) phases, separated by abrupt decadal-scale transitions. The DO cycle is commonly attributed to bistability in the Atlantic Meridional Overturning Circulation (AMOC), with stadial and interstadial periods corresponding to weak and strong overturning modes, respectively (6–8). North Atlantic sea ice is thought to play an important role in the DO cycle; it acts as a positive feedback amplifying variations in oceanic heat transport, sets the conditions for deep convection needed to sustain the overturning circulation, impacts atmospheric heat transport patterns, and insulates the wintertime atmosphere from the moderating influence of the ocean (9–16). Recent work suggests that the DO cycle is likely an internal oscillation of the coupled ocean–atmosphere–sea-ice system rather than externally forced via for example freshwater (17–20). The timing characteristics of the DO cycle depend on the background climate (21–23).

The most detailed records of the DO oscillation come from Greenland (Kalaallit Nunaat) ice cores, in which they were also first identified (24, 25). Here, we create a Greenland-wide reconstruction of the DO warming impact using four ice-core proxies. First, variations in water $^{18}O/^{16}O$ ratio ($\delta^{18}O$) of polar snow provide a well-established proxy for site temperature, with more isotopically depleted precipitation reflecting colder temperatures and vice versa (26, 27). Traditionally, this relationship is explained through

Author contributions: C.B., T.A.S., V.G., D.N., and J.W.C.W. designed research; C.B., T.A.S., K.N., T.B., V.G., M.H., C.H., T.R.J., H.A.K., J.B.L., J.A.M., V.M., D.N., S.O.R., L.C.S., J.P.S., A.S., B.H.V., and B.M.V. performed research; C.B., T.A.S., K.N., V.G., M.H., C.H., H.A.K., V.M., S.O.R., L.C.S., A.S., B.H.V., and B.M.V. analyzed data; T.A.S., K.N., T.B., V.G., M.H., C.H., T.R.J., H.A.K., J.B.L., J.A.M., V.M., D.N., S.O.R., L.C.S., J.P.S., A.S., B.H.V., B.M.V., and J.W.C.W. gave manuscript feedback; J.P.S. provided samples; and C.B. wrote the paper.

The authors declare no competing interest.

This article is a PNAS Direct Submission.

[1]To whom correspondence may be addressed. Email: christo.buizert@oregonstate.edu.

This article contains supporting information online at https://www.pnas.org/lookup/suppl/doi:10.1073/pnas.2402637121/-/DCSupplemental.

Published October 21, 2024.

Rayleigh distillation, in which vapor parcels undergo progressive isotopic depletion through rainout as they cool. Abrupt DO warming events show up as large positive $\delta^{18}O$ excursions in Greenland ice cores (Fig. 1 *A* and *D*), yet quantitative interpretation remains challenging because of concurrent changes in precipitation seasonality and vapor origin and pathways (28–30).

Second, the $^{15}N/^{14}N$ ratio ($\delta^{15}N$) in trapped atmospheric N_2 allows reconstruction of the change in site surface temperature during abrupt DO warming (31). Abrupt warming induces a temperature gradient between the surface snow and the 50 to 100 m deep lock-in depth where the air becomes isolated. This temperature gradient, in turn, drives thermal isotopic fractionation in which heavier N_2 isotopologs preferentially diffuse down-gradient causing $\delta^{15}N$ enrichment in closing bubbles. Due to the low thermal conductivity of firn, the temperature gradient will persist for several centuries causing a transient $\delta^{15}N$ excursion for each DO warming (Fig. 1 *C* and *F*). The magnitude of the excursion is proportional to the change in surface temperature ΔT_S, allowing the latter to be reconstructed—thereby calibrating the water-isotope thermometer. We use a firn densification model to disentangle the gravitational and thermal fractionation in the $\delta^{15}N$ data (32–34).

Third, water stable isotope deuterium excess ($d = \delta^2H - 8 \times \delta^{18}O$) reflects kinetic fractionation during evaporation, which depends on relative humidity over the ocean (35). More positive d is associated with both lower relative humidity and higher temperatures in source regions (36). The DO signal in d is strongly anticorrelated with $\delta^{18}O$ (Fig. 1 *B* and *E*), implying that during the cold DO stadials, Greenland vapor originates from warmer (i.e., more southerly) source regions.

Last, the observed annual-layer thickness in ice cores is a direct reflection of the past rate of snow accumulation, which is an important climatic and glaciological parameter (37). The effect of flow-induced thinning needs to be accounted for. Volcanic ice-core synchronization provides consistent annual-layer thickness records from multiple Greenland cores (38). We express snowfall changes as A_{GI}/A_{GS} or the ratio of Greenland interstadial and stadial accumulation rates.

Our compilation includes proxy data from seven Greenland ice cores that collectively provide good spatial coverage (Fig. 1*G* for core names and locations). For all four proxies, we rely on previously published data where available (34, 36, 38–44). Critically, we present 663 new $\delta^{15}N$ data points from the coastal eastern Renland (Fig. 1*C*) and southern Dye 3 (Fig. 1*F*) ice cores, that greatly expand spatial coverage of the ΔT_S reconstruction (*SI Appendix*, Figs. S1–S4). For each proxy (ΔT_S, $\Delta\delta^{18}O$, Δd, and A_{GI}/A_{GS}), we report its typical change across a DO warming transition from stadial to interstadial conditions, normalized to the average magnitude of DO events 5.2 through 8 (*Materials and Methods*). We find that the DO event magnitude in all Greenland proxies is independent of the background climate conditions, such as atmospheric CO_2 level, ice volume, and orbital configuration (*Materials and Methods*).

An important goal in climate science is to capture DO signatures in a fully coupled ocean-atmosphere general circulation model (GCM), both to benchmark model performance and to better describe and understand the underlying event dynamics. Water-isotope-enabled models can be compared directly to ice-core observations to assess whether the model correctly captures changes in sea ice, energy fluxes, and hydrology during the DO cycle. Here, we assess two such isotope-enabled model simulations of abrupt DO variability performed with the *i*HadCM3 (30), and *i*CESM1 (45) models. Both models rely on freshwater forcing (or hosing) to induce DO transitions. For the *i*HadCM3 model, we use an

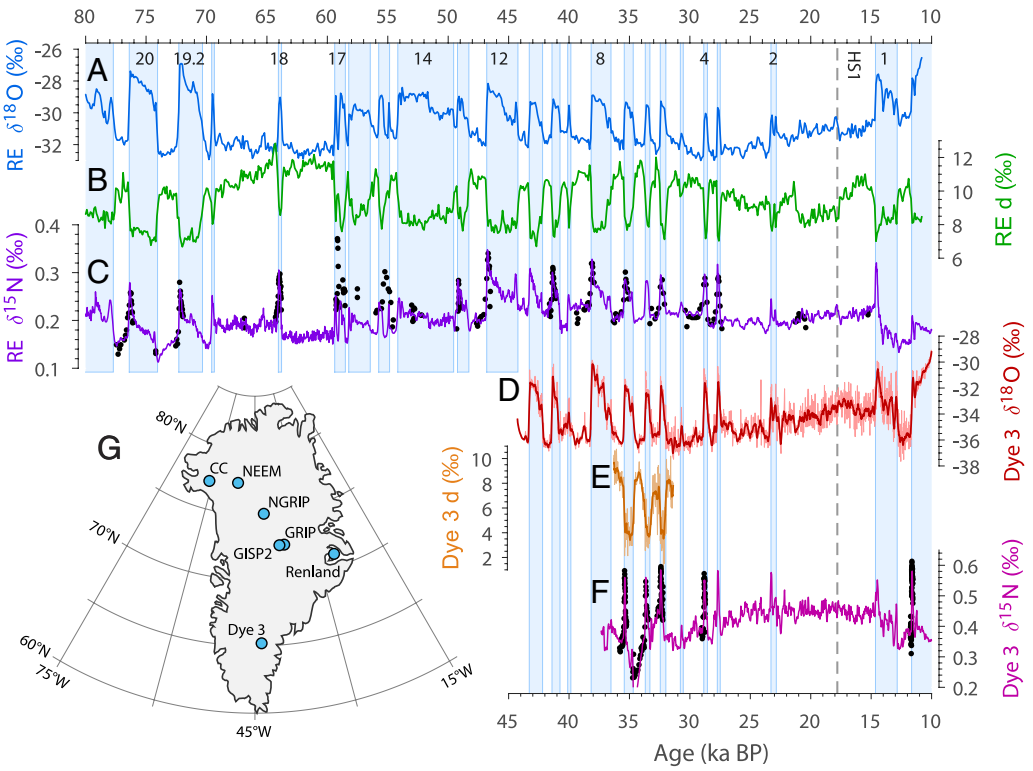

Fig. 1. Ice-core records of abrupt Dansgaard–Oeschger (DO) variability from the Renland and Dye 3 cores. (*A*) Renland $\delta^{18}O$. (*B*) Renland deuterium excess. (*C*) Renland $\delta^{15}N$ (black dots) with firn densification model fit (violet). (*D*) Dye 3 $\delta^{18}O$. (*E*) Dye 3 deuterium excess. (*F*) Dye 3 $\delta^{15}N$ (black dots) with firn densification model fit (fuchsia). (*G*) Greenland ice cores used in this study are Camp Century (CC), North Greenland Eemian Ice Drilling (NEEM), North Greenland Ice Core Project (NGRIP), Greenland Ice Core Project (GRIP), Greenland Ice Sheet Project 2 (GISP2), Dye 3, and Renland. Blue vertical shading denotes DO interstadials, with major interstadials numbered at the top; the vertical dashed line shows Heinrich Stadial 1 (HS1) onset.

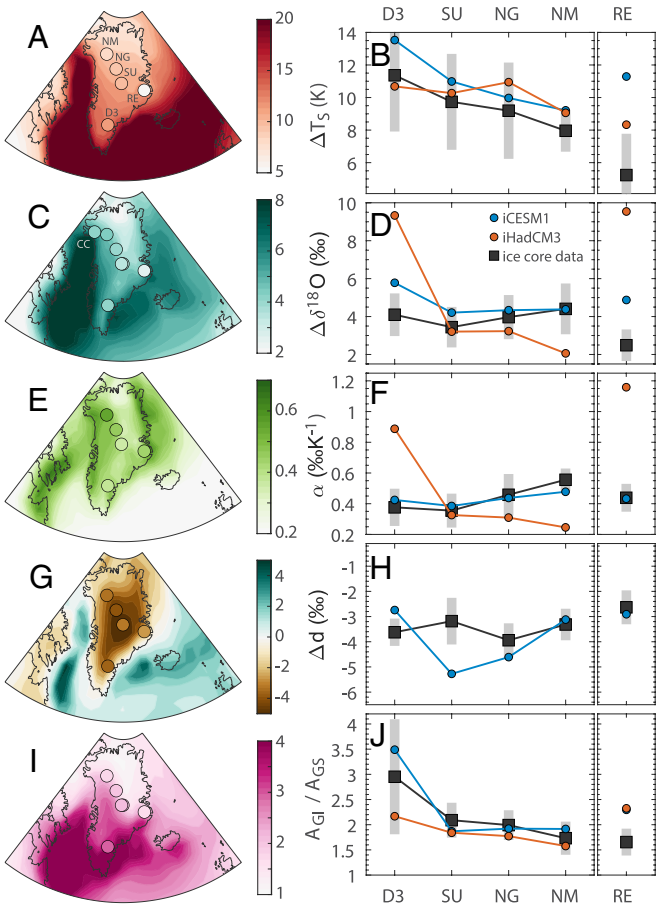

Fig. 2. Spatial fingerprint of abrupt DO warming in Greenland. (*A*) Change in surface temperature during a DO transition as simulated by the fully coupled iCESM1 model (background) and as derived from ice-core data (dots). (*B*) Change in surface temperature during a DO transition in a model-data comparison at five ice-core locations. The gray bars denote the ±1σ SD of the observations. (*C*) and (*D*) as panels (*A*) and (*B*), but for the change in precipitation $\delta^{18}O$. (*E*) and (*F*) as panels (*A*) and (*B*), but for the temporal isotope sensitivity α. (*G*) and (*H*) as panels (*A*) and (*B*), but for deuterium excess. (*I*) and (*J*) as panels (*A*) and (*B*), but for the interstadial-over-stadial ratio in snow accumulation rates. The five ice-core sites listed are Dye 3 (D3), Summit (SU, the average of GRIP and GISP2), NGRIP (NG), NEEM (NM), and Renland (RE).

ensemble of 15 DO events of varying magnitude, whereas *i*CESM1 simulates the two abrupt warmings associated with the last deglaciation that are relatively large in magnitude. We further use idealized experiments and moisture tagging in the isotope-enabled *i*CAM5 atmosphere-only GCM to further understand DO dynamics and hydrology.

Spatial Fingerprint of DO Warming Across Greenland

Our multiproxy reconstruction of the DO warming spatial fingerprint is shown in Fig. 2. The left panels show the proxy data on a map with the *i*CESM1 model simulations. The right panels show the same proxy data along a meridional transect from the Dye 3 core in the south to the NEEM core in the north; Renland core data are plotted to the right as this core is located on a separate ice cap on Greenland's east coast and not on the central north–south ice divide like the other cores. We first compare the data (gray square markers) to the *i*CESM1 and *i*HadCM3 models.

First, the DO warming magnitude ΔT_S shows a clear latitudinal gradient with the largest changes in the south (Fig. 2 *A* and *B*). This gradient was seen previously between Summit and NEEM (34, 40), and is here extended further south to Dye 3 where we observe the largest ΔT_S. The smallest changes are seen in Renland, which is perhaps unexpected given its close proximity to the North Atlantic. Both the *i*CESM1 and *i*HadCM3 models replicate the north–south pattern, though the latter has excess warming at NGRIP. This ΔT_S gradient has been seen previously in other models also (34, 46). Neither model simulates the small ΔT_S magnitude at Renland, possibly because the models lack the spatial resolution to resolve the steep topography of the region.

Second, the $\Delta\delta^{18}O$ is fairly constant at around 4‰ for core sites along the main ice divide, with a distinctly smaller value of 2.5‰ at Renland (Fig. 2 *C* and *D*). The more recent *i*CESM1 simulations show the most skill in fitting the $\Delta\delta^{18}O$ observations. Upon dividing the $\Delta\delta^{18}O$ by ΔT_S, we obtain the temporal isotope sensitivity α in units of $‰K^{-1}$ (Fig. 2 *E* and *F*). The *i*CESM1 simulations show a remarkable fit to the observations at all sites with the possible exception of NEEM. Both data and *i* CESM1 suggest a minimum in α at Greenland summit. The *i*HadCM3 simulations fit the data less well, chiefly due to the model-data offset in the simulated $\Delta\delta^{18}O$ (Fig. 2*D*).

Next, the Δd is fairly constant across Greenland with values of −3 to −3.5‰ (Fig. 2 *G* and *H*). The *i*CESM1 model simulates the correct sign and magnitude of the deuterium excess response, but produces a spatial pattern not seen in the data where the Δd magnitude is largest at Summit. Our study demonstrates that the DO *d* response can be correctly simulated in a coupled climate model. The *i*HadCM3 model has not been tuned to reproduce Greenland *d* and is omitted in this comparison.

Last, we assess the spatial pattern in the snow accumulation ratio A_{GI}/A_{GS} (Fig. 2 *I* and *J*). The observations are most accurate at the NGRIP core that has annual-layer counting, and the Summit and NEEM cores that have high-resolution volcanic synchronization to NGRIP (38, 47). Accumulation rates approximately double across a DO warming, with the largest increase seen at Summit. Both climate models capture the doubling, yet they disagree strongly on the signal in southern Greenland where data are more uncertain as annual layer thicknesses in the Dye 3 ice core are not adequately constrained.

Overall, we find that isotope-enabled coupled climate models have skill in simulating the climatic and hydrological response to the abrupt warming phase of the DO cycle, particularly the newer *i*CESM1 model. The *i*CESM1 model further provides the best fit to the low-latitude DO $\Delta\delta^{18}O$ response (*SI Appendix*, Fig. S12) as observed in a global network of speleothems (48).

Idealized Atmosphere-only Climate Model Experiments

DO warming events are associated with decreasing sea-ice concentration (SIC) and increasing sea-surface temperature (SST) in the North Atlantic. We perform a series of idealized climate model experiments to understand the relative importance of these two effects on Greenland climate and to identify the areas of the North Atlantic where such changes likely occurred. We use the atmosphere-only *i*CAM5 model, which is the atmospheric component of the *i*CESM1 model used in the model-data comparison. In these simulations, the surface ocean boundary conditions (SST, SIC) are prescribed. Rather than performing transient DO experiments, we run twelve 150-y snapshots under different idealized ocean boundary conditions. The difference between any two such snapshots is then compared to the corresponding shifts found in our observational database of DO signal magnitudes.

All idealized scenarios are created by applying SST or SIC anomalies to a monthly LGM climatology simulated with the coupled iCESM1 model (CTRL). The North Atlantic is divided

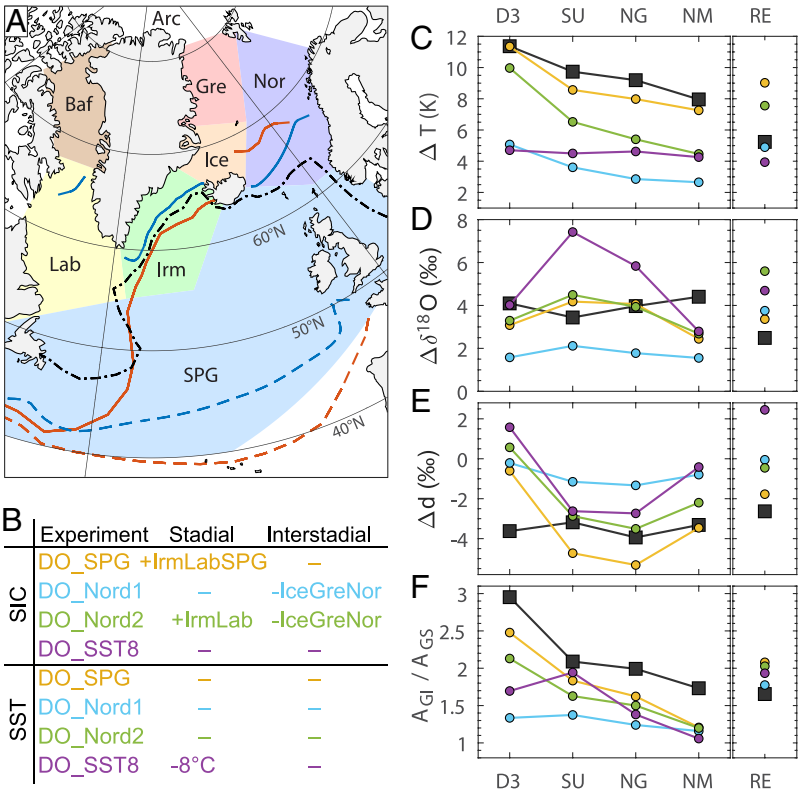

Fig. 3. Idealized climate model experiments of DO impact on Greenland. (*A*) Seas surrounding Greenland: Arctic Ocean (Arc), Baffin Bay (Baf), Labrador Sea (Lab), Greenland Sea (Gre), Iceland Sea (Ice), Irminger Sea (Irm), Norwegian Sea (Nor), and subpolar gyre (SPG). Simulated winter sea-ice edge (contour of 15% annual-mean SIC) for the LGM control run (black, dot-dashed), CESM1 stadial (blue dashed), CESM1 interstadial (blue solid), HadCM3 stadial (orange, dashed), and HadCM3 interstadial (orange, solid). (*B*) SIC and SST forcing in four representative idealized experiments (color coded). Indicated are changes relative to the LGM control. SIC anomalies reflect either adding (+) or removing (−) sea ice in the indicated marginal seas. (*C*) Change in surface temperature (ΔT) during a DO transition in a model-data comparison at five ice-core locations. Black square markers show the data, round markers four idealized iCAM5 experiments, color-coded as per panel (*B*). (*D*) As panel (*C*), but for the change in $\delta^{18}O$ ($\Delta\delta^{18}O$). (*E*) As panel (*C*), but for the change in deuterium excess (Δd). (*F*) As panel (*C*), but for the ratio of interstadial over stadial snow accumulation rates. Ice-core acronyms as in Fig. 2.

into different sectors that roughly correspond to the marginal seas (Fig. 3*A*), and SIC anomalies are applied to these individual sectors; SST anomalies are applied to the entire North Atlantic (*SI Appendix*, Supplement). Combining the twelve snapshots provides 66 idealized DO realizations (12 × 11 ÷ 2). *SI Appendix*, Fig. S10 provides a full evaluation; here, we discuss four representative scenarios. The SIC and SST forcing for stadial and interstadial conditions are given in Fig. 3*B*. The LGM climatology resembles the interstadial, rather than stadial, sea ice conditions simulated by the coupled models (Fig. 3*A*).

In a first scenario (DO_SPG), we use the control run as the interstadial state and the control run with winter sea ice added to the Irminger Sea, Labrador Sea, and subpolar gyre (SPG) as the stadial state. This simple scenario gives a good fit to the observations (Fig. 3 *C*–*F*), comparable to the fit obtained with the fully coupled models (Fig. 2). The next two scenarios (DO_Nord1 and DO_Nord2) investigate the common notion that the DO signals can be explained by SIC changes in the Nordic seas—i.e., not involving changes to the SPG. Here, the Nordic Seas are the combined Norwegian, Greenland, and Iceland Seas (Fig. 3*A*). In DO_Nord1, we use the control run as the stadial state and the control with sea ice in the Nordic seas removed (all seasons) as the interstadial state. In DO_Nord2, we make the stadial colder by further increasing seasonal SIC in the Irminger and Labrador Seas. Both these Nordic sea-ice scenarios simulate the correct sign of the proxy observations but do not match the magnitude. Last, for scenario DO_SST8, we use the control SIC for both stadial and interstadial snapshots, but we apply an 8 °C cooling to the stadial SST for all months. This scenario performs significantly worse than the DO_SPG and DO_Nord2 scenarios, particularly in failing to simulate the magnitude and spatial pattern of ΔT_S (Fig. 3*C*). For quantitative evaluation, model-data RMS differences are presented in *SI Appendix*, Fig. S10.

Moisture-tagging Climate Model Experiments

To better understand changes to moisture transport and Greenland water isotopes, our idealized simulations use moisture tagging in which the model tracks the region from which water vapor originates through the hydrological cycle. We track the vapor in Greenland precipitation back to a number of source regions—the source fractions for Greenland Summit are shown in Fig. 4*A* for stadial and interstadial conditions, respectively. Changes to the isotopic composition of Greenland precipitation primarily reflect a combination of two signals: 1) changes in fractionation during evaporation and transport to Greenland for each source region, and 2) changes to the vapor source distribution. As grouped here, the first of these two signals reflects both the kinetic fractionation during evaporation that is thought to control the *d* signal (35), as well as the Rayleigh distillation that controls the $\delta^{18}O$ and is commonly invoked to explain water-isotope variations in polar ice cores and to justify their use as a temperature proxy (27, 49). However, the second mechanism is expected to have a large imprint also, potentially biasing the isotope thermometer.

We apply a decomposition technique to separate the two main influences on precipitation $\delta^{18}O$ and *d*. The isotopes in precipitation at a given site (δ_p) represent the weighted sum of the contributions from all the tagged vapor source regions:

$$\delta_p = \sum_{i=1}^{N} [f_i \times \delta_i], \qquad [1]$$

where f_i is the fraction of the precipitation composed of vapor originating from tagged region i, and δ_i the isotope ratio of precipitation composed of vapor originating from region i. When considering anomalies in isotopes across a DO transition, change in isotopes $\Delta\delta_p$ can be written as:

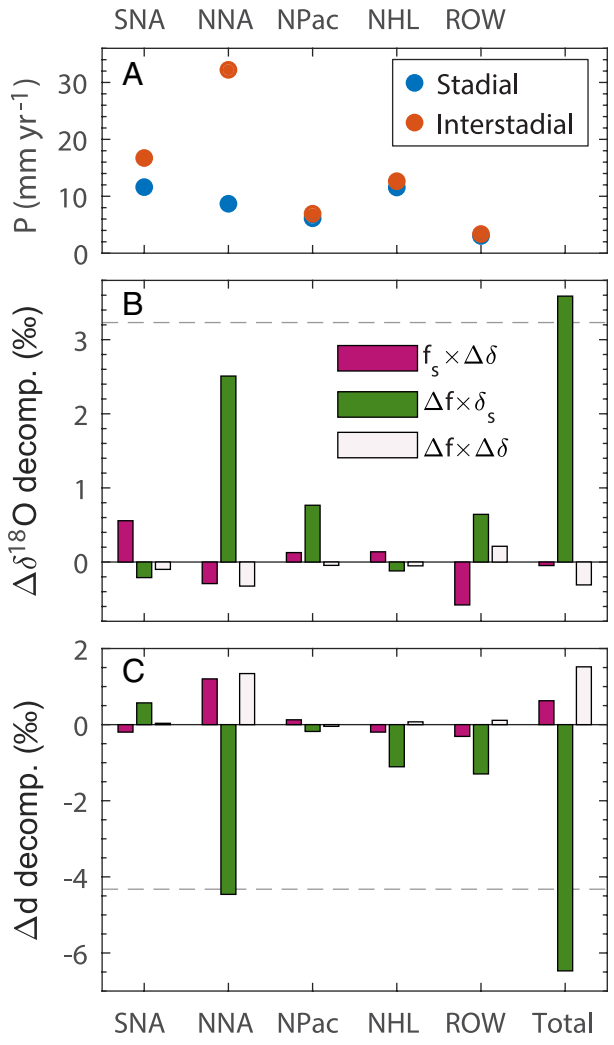

Fig. 4. Decomposition of Greenland isotope signals at Summit in the idealized iCAM5 DO_SPG experiment using moisture tagging. (*A*) Precipitation amounts contributed by tagged regions under stadial and interstadial conditions. SNA = southern North Atlantic, NNA = northern North Atlantic, NPac = North Pacific, NHL = Northern Hemisphere Land, ROW = rest of the world. (*B*) Decomposition of the change in δ^{18}O at Greenland Summit. (*C*) Decomposition of the change in deuterium excess at Greenland Summit.

$$\Delta\delta_p = \sum_{i=1}^{N}\left[f_i^S \times \Delta\delta_i\right] + \sum_{i=1}^{N}\left[\Delta f_i \times \delta_i^S\right] + \sum_{i=1}^{N}\left[\Delta f_i \times \Delta\delta_i\right], \quad [2]$$

where f_i^S and δ_i^S are the source fraction and precipitation isotope ratios under (pre-event) stadial conditions, and Δf and $\Delta\delta$ are the corresponding differences between interstadial and stadial conditions. The right-hand side has three terms. The first term represents changes to δ_i under unchanged (stadial) fractional vapor source contributions, the second term represents changes in the fractional source contributions under unchanged (stadial) δ_i, and the third term is the product of the two change terms and is therefore negligible in most cases as demonstrated in Fig. 4.

The isotope decomposition for the idealized DO_SPG scenario is shown in Fig. 4 *B* and *C*, where the pink, green, and white bars correspond to the three right-hand terms of Eq. **2**, respectively. We find that both for δ^{18}O and *d* the changes are strongly dominated by the changes in the vapor source fraction (green bars), in particular changes to the northern North Atlantic vapor region (NNA, defined as the Atlantic Ocean north of 45°N, or roughly the combination of the SPG and Nordic seas). Vapor contributions from this region are relatively heavy in δ^{18}O owing to their proximity to Greenland and have low *d* owing to their low source SST and high source relative humidity. During the stadial phase, this vapor source is suppressed by the presence of extensive SPG sea ice that acts as a "lid" to limit evaporation. Subsequently, during a DO warming transition the SPG sea ice is removed, increasing the fractional contribution of NNA vapor to Greenland thereby shifting the ice-core signals toward the NNA end-member (more positive δ^{18}O and more negative *d*). Our analysis suggests that the changes in NNA vapor contribution, driven by variations in SPG sea-ice cover, are the most important driver of the observed shifts in Greenland ice-core water-isotope ratios across DO events. By contrast, changes to fractionation en route (including Rayleigh distillation) do not contribute strongly to the DO water-isotope shifts (pink bars). To clarify: Rayleigh distillation strongly contributes to water-isotope depletion in Greenland during both stadial and interstadial phases, yet in our simulations, the shifts seen across DO events are not driven by changes in the degree of Rayleigh distillation.

Discussion

From our idealized atmosphere-only climate model simulations, we conclude that seasonal sea ice in the SPG is a sufficient condition to explain, to first order, all the ice-core observations. In fact, the scenarios that perform best all have seasonal sea ice in the SPG under stadial conditions (*SI Appendix*, Supplement). In our experiments, stadial SPG sea ice is therefore both a sufficient and a necessary condition to explain the Greenland observations. However, we cannot rule out that other models are able to fit the Greenland DO observations without SPG sea ice. While sufficient to explain the Greenland observations, seasonal SPG sea ice by itself is insufficient in driving the low-latitude $\Delta\delta^{18}$O DO signature observed in speleothems (*SI Appendix*, Fig. S12) which additionally requires the (global) SST anomalies associated with the thermal bipolar seesaw.

While the Nordic Seas are often cited as a key location for DO activity (14, 50–52), our simulations suggest that sea-ice changes in the Nordic seas alone are insufficient to explain the observations—in particular, the DO_Nord1 and DO_Nord2 scenarios fall short of the observed magnitude of the ΔT_S and A_{GI}/A_{GS} responses (Fig. 3 *C* and *F*). Moreover, these scenarios were designed to have maximum climate response by fully removing interstadial Nordic sea ice during all seasons. This contradicts observations of seasonal sea ice in the Norwegian Sea during interstadials (14). Modifying the DO_Nord1 and DO_Nord2 scenarios to include more realistic seasonal sea ice in the interstadial Nordic Seas would reduce the signal magnitude in Greenland, further degrading the model fit to observations. While we do not mean to dispute that Nordic Sea SIC and SST vary across the DO cycle, we argue that those changes alone are insufficient and need to be accompanied by changes to the SPG seasonal sea ice.

The observations from our idealized scenarios are consistent with DO changes in sea-ice extent simulated in the coupled climate models. Both coupled models simulate seasonal sea ice covering most of the SPG under stadial conditions (Fig. 3*A*, dashed lines), and seasonal sea ice remaining in most of the Nordic Seas under interstadial conditions (solid lines). Qualitatively similar sea-ice changes are simulated in a recent study (21) with a coupled model that exhibits spontaneous DO oscillations (not shown). The coupled models employed here apply freshwater flux anomalies to the North Atlantic ("hosing") to induce DO transitions; the fact that comparable sea-ice changes are simulated for different DO triggering mechanisms suggests this finding to be robust.

Changes in SST appear to play a minor role by themselves in explaining the Greenland ice-core DO signal—other than their role in forcing SIC. Even by imposing an extremely large SST anomaly of 8 °C in the North Atlantic, it is impossible to match the magnitude of the observed changes in ΔT_S. We find that North Atlantic SIC thus has a much greater impact than SST on Greenland climate. This is due to the fact that wintertime sea ice can insulate the atmosphere from the moderating influence of the relatively warm ocean waters, allowing for much colder air temperatures in the circum-North Atlantic. This effect does not occur in summer, and DO stadial cooling is therefore mainly a wintertime effect (53, 54).

The moisture-tagging experiments provide new insights into the drivers of Greenland isotopic abundances ($\delta^{18}O$ and d) during the DO cycle. In the traditional water isotope interpretation, based on 1-D Rayleigh distillation, Greenland $\delta^{18}O$ reflects the source-site temperature difference and d reflects the source SST (36, 49). For the DO_SPG scenario, in which SST is constant, the traditional 1-D interpretation would give a $\Delta\delta^{18}O$ that reflects the stadial-interstadial change in site temperature only. Our 3-D isotope transport modeling refutes this traditional interpretation. Our analysis suggests that the stadial-period suppression of vapor from the SPG due to enhanced SIC can explain nearly the entire shift in Greenland $\delta^{18}O$ and d. Effectively, a more expansive sea-ice extent in the North Atlantic acts like a "lid" for evaporation, which dramatically reduces the amount of North Atlantic vapor from the SPG region that reaches Greenland. This reduces the relative contribution of the northern North Atlantic's high-$\delta^{18}O$, low-d end-member to Greenland precipitation. Our findings align well with a more recent conceptual framework in which isotopic ratios are explained via the balance of evaporation and precipitation along the moisture pathway (55). It also agrees with an earlier isotope-enabled modeling study of DO events that argued that abrupt changes in SIC, and not site temperature, control $\delta^{18}O$ (30). Note that the analysis presented here only applies to isotope changes across abrupt DO events. On other timescales and for other Greenland climate drivers (e.g., orbital and greenhouse gas forcing), as well as in Antarctica, temperature-driven Rayleigh distillation likely does represent an important control on observed variations in ice-core water isotopes. Practically, Greenland water isotopes can still be used as a qualitative proxy for local climate given that $\delta^{18}O$ and T_S are strongly correlated through their shared dependence on North Atlantic sea ice conditions.

Previous studies have inverted isotope models to use $\delta^{18}O$ and d together as independent variables to reconstruct both site and vapor source temperatures (42, 56). Our moisture-tagging experiments suggest this approach may be invalid across DO events. We find that $\delta^{18}O$ and d have the same driver, namely variations in the vapor contribution from the SPG region. Therefore, these two proxies cannot be used to infer two independent climate parameters. The fact that $\delta^{18}O$ and d respond to a single driver does provide a compelling reason for their strong correlation across the DO cycle on multidecadal timescales (Fig. 1 *A-B*). However, decadal-scale timing differences between the $\delta^{18}O$ and d signals are observed for DO transitions, that cannot be explained via this covariance alone (25). Note that Δd may still (qualitatively) reflect source SST, with the negative shift across a DO warming consistent with an effective northward shift in mean vapor-source latitude from warmer Southern North Atlantic (SNA) to colder NNA sources.

Besides the DO mode of abrupt climate variability, the North Atlantic further experiences the Heinrich mode of abrupt change (57). However, the latter mode does not impact Greenland isotopes or temperatures strongly (41) and our methodology therefore does not allow us to investigate sea-ice changes during Heinrich stadials.

Conclusions

We have compiled new and previously published data from seven Greenland ice cores to derive a Greenland-wide, multiproxy signature of abrupt DO warming events. The four proxies in our compilation are the changes in surface temperature, water $\delta^{18}O$, deuterium excess, and accumulation. We compare our compiled data to isotope-enabled ocean-atmosphere coupled transient climate model simulations of abrupt DO events, and find that the models have skill in fitting the observations. We conducted a series of idealized isotope-enabled atmosphere-only climate model simulations and compared them against the observations to show that stadial-period seasonal sea-ice cover of the North Atlantic subpolar gyre is a sufficient, and likely also a necessary condition to explain DO variability in Greenland. In our experiments, changes to the Nordic Seas alone are insufficient to fit the observations. Likewise, sea-surface temperature warming alone (i.e., not accompanied by sea-ice changes) is insufficient to fit the observations. Moisture-tagging experiments suggest that the observed isotopic changes in both $\delta^{18}O$ and deuterium excess can be explained almost completely via stadial-period suppression of vapor from the northern North Atlantic due to the presence of extended sea ice. These experiments further suggest that changes in the site-temperature-driven Rayleigh distillation do not contribute significantly to the Greenland isotopic shifts across the DO cycle, refuting the traditional interpretation of the water isotope thermometer on this timescale. Our study provides a comprehensive, multiproxy, data-model synthesis of abrupt DO climate variability in Greenland. The database will be a valuable target for benchmarking future climate model studies that seek to simulate abrupt DO events.

Materials and Methods

Description of Ice Cores and Timescales. Drilling of the Dye 3 ice core (as part of the Greenland Ice Sheet Project) was finished in 1981 (58–60). Cores were cut vertically with parallel half-cores divided between the US (cut into 1 m tubes) and Denmark (cut into 0.55 m bags). Upon the retirement of Chester Langway, many of the US tubes were shipped from Buffalo, NY, to Copenhagen, Denmark. The core sections used in this study are all currently archived in Copenhagen but came from both the US and Danish ice allocations. For the Dye 3 ice age scale, we use a published chronology for the Holocene section (61) and extend it into the glacial using tie points to other Greenland ice cores based on water $\delta^{18}O$ and volcanic deposits (*SI Appendix*, Data supplement S01). Ages are given on the 2005 Greenland Ice Core Chronology (GICC05). At face value, it appears that Dye 3 $\delta^{18}O$ can be matched to other Greenland cores back to DO11 (43 ka BP, 1,918 m depth). However, closer examination of gas records ($\delta^{15}N-N_2$, CH_4) suggests the first stratigraphic disturbance (62, 63), likely overturned folds, may occur already at DO8 (38 ka BP, 1,895 m depth). Here, we refrain from interpreting Dye 3 data deeper than 1,890 m.

The RECAP (Renland ice cap project) ice core was drilled in 2015 to a depth of 562 m, into the last interglacial (64). The RECAP glacial chronology was constructed by matching of dust and water $\delta^{18}O$ abrupt signatures.

For all other ice cores, we use published ice age timescales (38).

Ice-core $\delta^{15}N$-N_2 Data. The ice-core $\delta^{15}N$ was measured on the RECAP and Dye 3 (US 1 m tube sections) ice cores in the ice-core gas laboratory at Pennsylvania State University, USA, and on the Dye 3 core at the University of Copenhagen, Denmark.

The Pennsylvania State University measurements were performed on discrete ice samples. Briefly, samples of ~15 g were melted under vacuum, transferred through a trap submerged in liquid nitrogen, and trapped in a sample dip tube submerged in liquid helium. Samples are then introduced into a dual-inlet isotope ratio mass spectrometer (IRMS) for $\delta^{15}N$ isotopic analysis and reported using contemporary atmospheric N_2 as a standard.

The University of Copenhagen measurements were performed using a continuous flow analysis melter system with a gas extraction membrane (65), connected

to a Thermo Delta V IRMS operating in continuous flow mode (66). The continuous data were averaged into 4 cm bins. Drift in the IRMS instrument was corrected for by applying a depth-variable offset determined via comparison to the aforementioned discrete $\delta^{15}N$ data. We choose to only interpret the continuous $\delta^{15}N$ data for DO events 7, 6, 5.2, 4, and the Holocene onset; at these depths, discrete $\delta^{15}N$ data are available to assess the offset. A comparison between the discrete and continuous $\delta^{15}N$ data suggests a good agreement (*SI Appendix*, Fig. S4).

A total of 267 new $\delta^{15}N$ data points are presented for Renland (all Penn State University), and 396 new $\delta^{15}N$ data points for Dye 3 (244 from Penn State University, 152 from University of Copenhagen). Data are available via refs. 67, 68.

For all other ice cores, we rely on previously published $\delta^{15}N$-N_2 data as available (34, 39–41, 69).

Ice-core Water-isotope Analysis. Dye 3 (Danish 0.55 m tube sections) ice-core water $\delta^{18}O$ was measured in Copenhagen using the University of Colorado continuous-flow analysis (CFA) setup (70). In our analysis, we average the previously published Dye 3 water $\delta^{18}O$ (58), and the new continuous measurements. Data are provided in the *SI Appendix*, Data Supplement S01. For Dye 3 deuterium excess, we use previously published data (36).

For all other cores, we rely on previously published water-isotope ($\delta^{18}O$ and d) data (42, 44, 71, 72).

Ice-core Methane Analysis. Dye 3 atmospheric methane (CH_4) mixing ratios were measured in Copenhagen using the University of Copenhagen CFA setup (65). The CH_4 data were used to detect the depth range of the abrupt DO transitions in the gas phase to enable targeted discrete sampling for $\delta^{15}N$-N_2.

Reconstructing ΔT_s using Firn Densification Modeling. Firn densification modeling is used to reconstruct ΔT_S from the $\delta^{15}N$ data. For the Dye 3 and Renland data, we run a coupled dynamical densification-heat transport model (34, 41, 73, 74) that simulates the thermal and gravitational fractionation of $\delta^{15}N$ in closed bubbles as a function of the site $T_S(t)$ and $A(t)$ histories (*SI Appendix*, Figs. S1–S4). The site forcing histories are initially based on the water-isotope $\delta^{18}O$ record, but then optimized (or calibrated) using an automated algorithm to minimize the model-data misfit to the $\delta^{15}N$ data. Note that this approach remains valid despite our observation that T_S-controlled Rayleigh distillation is not the main driver of the $\delta^{18}O$ variations on DO timescales; there is a strong T_S-$\delta^{18}O$ correlation via their shared dependence on sea ice. The densification model is implemented with different mathematical descriptions of firn densification physics. For the Renland modeling, we use a dynamical formulation of the Herron–Langway model (75); at the Dye 3 site, we use the Barnola–Pimienta model instead as it seems to provide a better fit to the $\delta^{15}N$ data in this high-accumulation setting (76). Previous work (34) has shown that different physical descriptions of the firn densification physics yield values of ΔT_S that are identical within uncertainty. Model code is archived in ref. 77.

Due to the poor chronological constraints at both Dye 3 and Renland, the gas-age–ice-age difference, inferred from the depth offsets between the DO transitions in $\delta^{18}O$ and $\delta^{15}N$, is not very reliable. This results in errors in the absolute $T_S(t)$ and $A(t)$ histories obtained, and hence these are not interpreted. For example, the long-term trends in reconstructed (stadial) $T_S(t)$ at Dye 3 and Renland are not robust, nor are T_S differences between successive stadials or $T_S(t)$ trends within stadials. However, relative DO warming magnitudes ΔT_S are well constrained via the transient excursions in $\delta^{15}N$ caused by thermal isotopic fractionation. The ΔT_S estimates are extracted from the $\delta^{15}N$-based T_S histories. For Dye 3 and Renland, we use the ones described here; for the other sites, we use published histories for NGRIP (39), NEEM (47), and GISP2 (41).

The caveats for the ΔT_S estimates also apply to the reconstructed isotope sensitivities α. These strictly apply only to the abrupt transitions themselves, and cannot be used to make inferences about long-term climate change or the relative temperatures of successive stadials.

Compiling the Multiproxy DO Event Database. We extract the DO change magnitudes from the following four records: i) ΔT_S, ii) $\delta^{18}O$, iii) d, and iv) annual layer thickness (for past accumulation rate). We used a similar methodology for all records and all sites. First, we identify the midpoints of all the DO warming transitions. Next, we define 400-y pre-event, and 150-y postevent averages at fixed intervals relative to the event midpoints. The pre-event averaging period is longer, because stadial climates tend to have greater signal variance, and because several of the DO events are of short duration. To avoid the transition itself, the pre-event period ends 60 y prior to the midpoint and the postevent period starts 30 y after this midpoint. The pre- and postevent periods are evaluated by hand for all events and all cores and adjusted manually where necessary, for example in the case of a very short-duration DO (inter)stadials, data gaps, unusually sharp/gradual transitions, etc. The change magnitude is taken to be the difference between the post- and pre-event averages–except for the annual layer thickness where we take the ratio. The NGRIP $\Delta\delta^{18}O$ amplitudes we find agree well ($r = 0.92$, $P < 10^{-12}$) with independent estimates thereof (78).

In reconstructing DO accumulation rate changes, we use the average annual layer thickness in the pre- and postevent averaging windows. We do not apply a correction for layer thinning due to ice flow. Because the pre- and postevent depth ranges are close together in depth, we expect them to have experienced the same degree of thinning. When calculating their ratio, the thinning function cancels. For the Dye 3 and Renland cores, we lack the detailed volcanic matching to assess annual layer thickness, and instead, we have to rely on an alternative approach in which we use the average annual layer thickness during entire (inter-) stadial phases as found from matching the climatic $\delta^{18}O$ transitions. Using the four volcanically cross-dated cores (NGRIP, GISP2, GRIP, and NEEM), we assess how much this alternative approach differs from the optimal approach and linearly scale the Dye 3 and Renland observations to correct for this bias. For the Dye 3 core, we find large spread in the A_{GI}/A_{GS} ratio, which likely reflects nonmonotonic thinning due to the complex ice flow history of the site, and possibly the development of large-scale disturbances in the stratigraphy prior to their overturning by simple shear to produce folds (63).

We assess a total of 34 DO warming events (from the Holocene onset to DO 25). Data availability is nonuniform, with data gaps existing for most cores and most proxies. To derive meaningful site averages in the presence of data gaps, we take the following approach. For each proxy, we define a reference dataset, which is the average of the NGRIP and summit cores where data coverage is best (for $\delta^{18}O$ and A where data from both summit cores are available, we first average them). Next, we divide each DO event magnitude by that same event in the proxy reference dataset, thereby expressing its relative magnitude. Now, for each combination of core and proxy, we average over all the available events, thereby obtaining the average relative strength. To convert this back to a typical absolute event magnitude, we multiply by the average of DO events 5.2 through 8 as a normalization step. Due to differences in data coverage, we assess the Holocene onset and DO events 1 through 13 for ΔT_S, the Holocene onset and events 1 through 23.1 for $\Delta\delta^{18}O$, the Holocene onset and events 1 through 21.1 for Δd, and the Holocene onset and events 1 through 17.2 for A_{GI}/A_{GS}.

Overall, we find the Greenland proxies to be correlated with each other (*SI Appendix*, Fig. S5), although the slopes and intercepts vary between the coring sites. We do not find meaningful trends through time of the regression slopes. The patterns we see in the multievent averages are also reflected in most of the individual events, though with more scatter particularly in the ΔT_S reconstructions that are technically most challenging (*SI Appendix*, Fig. S6). However, it is also conceivable that the spatial patterns associated with each individual event may deviate from the multievent average.

Last, we assess whether the DO warming magnitude in the various proxies is correlated with background climate conditions, here CO_2 (79), benthic $\delta^{18}O$ (80) (a proxy for global ice volume and climatic conditions), orbital obliquity (81), and orbital precession index (*SI Appendix*, Fig. S7). We find no consistent correlations between Greenland DO event magnitude and background climate, as previously already observed independently for NGRIP $\Delta\delta^{18}O$ (78). For each panel in *SI Appendix*, Fig. S7, there are more cores that suggest no statistically significant correlation ($P > 0.05$) than cores that do suggest a correlation ($P < 0.05$). Between the 7 cores, 5 proxies, and 4 background climate parameters, there are 112 combinations where we have data available to calculate a correlation. Out of these 112, we find only four instances where $P < 0.05$ (in line with expectations from chance alone). These four instances are distributed across different Greenland proxies, core sites, and background conditions. Two out of the four are related to a single proxy event, namely the large $\Delta\delta^{18}O$ signal of DO 19.2. Based on these analyses, we conclude that background climate conditions do not impact the magnitude of Greenland DO events in the proxies we investigate. An earlier study suggested a correlation between obliquity and the isotope sensitivity α on orbital timescales–(39) our analysis suggests this correlation does not apply to millennial timescales. Assessed event magnitudes are archived in ref. 82.

Climate Models. In this study, we use three isotope enabled climate models. For the *i*CESM1 and *i*HadCM3 models, we rely on previously published simulations (30, 45); for the *i*CAM5 model, we performed new simulations as described below. An assessment of the performance of the *i*CESM1 and *i*HadCM3 models can be found elsewhere (83–85). For the iCAM5 atmosphere-only simulations we introduce here, and the iCESM1 coupled model simulations they are based on, we provide a data-model comparison for the PI and LGM in Greenland (*SI Appendix*, Fig. S11). Both models capture the PI surface temperature well, but have a warm T_S bias during the LGM (*SI Appendix*, Fig. S11, left column) that we attribute to the strong LGM overturning in the model (note that the simulated LGM state more closely resembles the interstadial than the stadial DO mode; see Fig. 3*A*). Both models capture the Greenland spatial $\delta^{18}O$ pattern well during both PI and LGM conditions (*SI Appendix*, Fig. S11, center column) though with a constant +10‰ offset. Such offsets are commonly observed in isotope-enabled models over the polar ice sheets (86–89), and its constancy suggest it should not strongly impact the isotopic $\Delta\delta^{18}O$ differences we interpret here. As in other models, the simulated deuterium excess has a negative bias of a few ‰, yet insufficient ice core data are available to robustly assess the model response. It is unclear how this bias in absolute d values impacts the relative Δd changes that we interpret.

For all three models, we furthermore provide a comparison of the global response in $\delta^{18}O$ of precipitation across a rapid DO warming transition (*SI Appendix*, Fig. S12) to data from Greenland ice cores (this study) and a global database of speleothems (48). The *i*CESM1 simulation provides the best fit to global data. The *i*CAM5 DO_SPG simulation provides a good fit to Greenland $\Delta\delta^{18}O$, yet it lacks a strong global response as its forcing is very localized and does not include global SST anomalies associated with the bipolar seesaw. The *i*HadCM3 simulation uses a global negative freshwater anomaly to compensate for the North-Atlantic hosing that has an unrealistic imprint on global surface-ocean $\delta^{18}O$. This results in unrealistically negative $\Delta\delta^{18}O$ across the DO simulation; water-isotope ratios in these DO simulations should not be interpreted outside of Greenland. CESM model output is archived in ref. 90.

Idealized iCAM5 Simulations. Here, we use the isotope-enabled Community Atmosphere Model 5 (*i*CAM5), which is part of the Community Earth System Model 1.2 (CESM 1.2) (84, 91). The model has a nominal 2-degree resolution, with a 96×144 latitude-by-longitude grid, and with 30 vertical levels. Precipitation water-isotope simulations in iCESM have been shown to have considerable skill in fitting observations (92).

In our idealized simulations, the atmosphere-only *i*CAM5 model was run for 200 y, with the first 50 y discarded as the model spin-up. The remaining 150 y are averaged to obtain a monthly climatology. Instead of simulating DO events in a transient manner, we use two equilibrium snapshot simulations–one representing the climate state before, and one after, the abrupt transition. We interpret the difference between two such scenarios as the event magnitude (16, 93). We emphasize that these are idealized scenarios, and therefore simplified and sometimes thermodynamically inconsistent.

All scenarios start from an LGM control run (CTRL), that is obtained from the coupled CESM1 model (94). Including the control run (CTRL), we here interpret 12 scenarios. All scenarios involve anomalies applied to the CTRL. Seven scenarios include only SIC anomalies–three negative and four positive anomalies (*SI Appendix*, Fig. S8). Two scenarios involve only SST anomalies (4 °C and 8 °C of North Atlantic cooling). Two scenarios involve a combination of SIC expansion and SST anomalies (1 °C and 2 °C of North Atlantic cooling). In terms of North Atlantic conditions, the LGM control more closely resembles the interstadial conditions as simulated by the coupled models (Fig. 3*A*), even though the LGM climate is typically considered to be in the stadial mode. Explanations include the possibility that the model underestimates North Atlantic LGM sea ice, or that the LGM had warmer North Atlantic conditions than the typical DO stadial did.

SST cooling anomalies are applied across the North-Atlantic to all months. For SIC removal scenarios, SIC in a selected area is removed in all months, after which we apply 2-D smoothing to prevent abrupt SIC transitions. For SIC addition scenarios, SIC is applied to a selected area, using a SIC seasonality that is derived from the Nordic seas SIC seasonality of the CTRL (*SI Appendix*, Fig. S9*A*). Again, we apply 2-D smoothing to prevent abrupt SIC transitions. To prevent the physically unrealistic situation of sea ice on top of warm waters, we further apply an SST anomaly in all grid cells that have a positive SIC anomaly applied. First, we apply a second-order polynomial fit to the North-Atlantic SST-SIC scatter plot (*SI Appendix*, Fig. S9*B*). Next, we calculate the SST anomaly in each grid cell as the product of: 1) the difference in SIC fraction between the scenario and the CTRL (a number between 0 and 1), and 2) the temperature difference between the CTRL and the SST implied by the second-order polynomial fit.

The 12 scenarios give a total of 66 pairs (12 × 11 ÷ 2) that are interpreted as potential DO event realizations. For each pair, we use the scenario with colder Greenland temperatures as the stadial. Next, we calculate the rmsd between the model and the observational database for each of the four proxies (*SI Appendix*, Fig. S10). For each proxy, the best performing DO realizations are outlined with thick black lines; The four idealized scenarios outlined in Fig. 3 are color-coded. Overall, the best model-data agreement is observed for scenario DO_SPG (Fig. 3). This scenario uses the CTRL as the interstadial, extended seasonal sea ice in the SPG as the stadial and no SST changes.

Data, Materials, and Software Availability. Data and model code are publicly archived (67–69, 77, 82, 90). Dye 3 timescale and isotope record are included in the Dataset S1.

ACKNOWLEDGMENTS. We thank Edward Brook, Kaden Martin, and Markus Jochum for useful discussions; Chester Langway, Willi Dansgaard, and others for archiving the Dye 3 ice core for future use; and the New York 109th Air National Guard for airlift in Greenland. The RECAP (Renland) ice coring effort was financed by the Danish Research Council through a Sapere Aude Grant, the U.S. NSF through the Division of Polar Programs, the Alfred Wegener Institute, and the European Research Council under the European Community's Seventh Framework Programme (FP7/2007-2013)/ERC Grant agreement 610055 through the Ice2Ice project and the Early Human Impact project (267696). We gratefully acknowledge financial support from the U.S. NSF (awards 1804154, 1804133, 2102944, and 1804098), the European Commission Horizon 2020 TiPES project (Grant agreement 820970), and the Danish Research Foundation (DFF 1131-00007B). Four anonymous reviewers provided detailed and constructive feedback that improved the manuscript. Parts of this manuscript were written while actually flying over Greenland on Delta Airlines flight 178 from Portland to Amsterdam.

Author affiliations: [a]College of Earth, Ocean and Atmospheric Sciences, Oregon State University, Corvallis OR 97331; [b]The Earth and Environmental Systems Institute, Pennsylvania State University, University Park, PA 16802; [c]Department of Earth, Environmental & Planetary Sciences, Rice University, Houston, TX 77005; [d]Physics of Ice, Climate and Earth, Niels Bohr Institute, University of Copenhagen, Copenhagen Ø 2100, Denmark; [e]University of Tasmania, Institute for Marine and Antarctic Studies, Hobart, TAS 7001, Australia; [f]Rosenstiel School of Marine, Atmospheric, and Earth Science, University of Miami, Coral Gables, FL 33149; [g]Institute of Arctic and Alpine Research, University of Colorado, Boulder, CO 80303; [h]Climate Science Centre, CSIRO Environment, Aspendale, VIC 3195, Australia; [i]Australian Antarctic Program Partnership, Institute for Marine and Antarctic Studies, Hobart, TAS 7001, Australia; [j]Department of Physics, University of Auckland, Auckland 1142, Aotearoa, New Zealand; [k]British Antarctic Survey, Cambridge CB3 0ET, United Kingdom; and [l]College of Arts and Sciences, University of North Carolina, Chapel Hill, NC 27599

1. A. Robinson, R. Calov, A. Ganopolski, Multistability and critical thresholds of the Greenland ice sheet. *Nat. Clim. Change.* **2**, 429–432 (2012).
2. P. deMenocal *et al.*, Abrupt onset and termination of the African Humid Period: Rapid climate responses to gradual insolation forcing. *Quat. Sci. Rev.* **19**, 347–361 (2000).
3. D. I. Armstrong McKay *et al.*, Exceeding 1.5°C global warming could trigger multiple climate tipping points. *Science* **377**, eabn7950 (2022).
4. W. Dansgaard *et al.*, Evidence for general instability of past climate from a 250-kyr ice-core record. *Nature* **364**, 218–220 (1993).
5. B. Birner, D. A. Hodell, P. C. Tzedakis, L. C. Skinner, Similar millennial climate variability on the Iberian margin during two early Pleistocene glacials and MIS 3. *Paleoceanography* **31**, 203–217 (2016).
6. H. Stommel, Thermohaline convection with two stable regimes of flow. *Tellus* **13**, 224–230 (1961).
7. S. Rahmstorf, Ocean circulation and climate during the past 120,000 years. *Nature* **419**, 207–214 (2002).
8. J. Lynch-Stieglitz, The atlantic meridional overturning circulation and abrupt climate change. *Annu. Rev. Marine Sci.* **9**, 83–104 (2017).
9. C. Li, A. Born, Coupled atmosphere-ice-ocean dynamics in Dansgaard-Oeschger events. *Quat. Sci. Rev.* **203**, 1–20 (2019).
10. H. Gildor, E. Tziperman, Sea-ice switches and abrupt climate change. *Philos. Trans. R. Soc. Lond. Ser. A: Math., Phys. Eng. Sci.* **361**, 1935–1944 (2003).
11. L. C. Menviel, L. C. Skinner, L. Tarasov, P. C. Tzedakis, An ice–climate oscillatory framework for Dansgaard-Oeschger cycles. *Nat. Rev. Earth Environ.* **1**, 677–693 (2020).
12. G. Vettoretti, W. R. Peltier, Fast physics and slow physics in the nonlinear Dansgaard-Oeschger relaxation oscillation. *J. Clim.* **31**, 3423–3449 (2018).

13. W. S. Broecker, Abrupt climate change revisited. *Global Planet. Change* **54**, 211–215 (2006).
14. H. Sadatzki *et al.*, Rapid reductions and millennial-scale variability in Nordic Seas sea ice cover during abrupt glacial climate changes. *Proc. Natl. Acad. Sci. USA* **117**, 29478–29486 (2020).
15. N. Maffezzoli *et al.*, A 120,000-year record of sea ice in the North Atlantic?. *Clim. Past* **15**, 2031–2051 (2019).
16. C. Li, D. S. Battisti, C. M. Bitz, Can North Atlantic Sea ice anomalies account for Dansgaard-Oeschger climate signals? *J. Clim.* **23**, 5457–5475 (2010).
17. W. R. Peltier, G. Vettoretti, Dansgaard-Oeschger oscillations predicted in a comprehensive model of glacial climate: A "kicked" salt oscillator in the Atlantic. *Geophys. Res. Lett.* **41**, 2014GL061413 (2014).
18. Y. Kuniyoshi, A. Abe-Ouchi, S. Sherriff-Tadano, W.-L. Chan, F. Saito, Effect of climatic precession on Dansgaard-Oeschger-like oscillations. *Geophys. Res. Lett.* **49**, e2021GL095695 (2022).
19. X. Zhang *et al.*, Direct astronomical influence on abrupt climate variability. *Nat. Geosci.* **14**, 819–826 (2021).
20. I. Malmierca-Vallet, L. C. Sime, Dansgaard-Oeschger events in climate models: Review and baseline Marine Isotope Stage 3 (MIS3) protocol. *Clim. Past* **19**, 915–942 (2023).
21. G. Vettoretti, P. Ditlevsen, M. Jochum, S. O. Rasmussen, Atmospheric CO2 control of spontaneous millennial-scale ice age climate oscillations. *Nat. Geosci.* **15**, 300–306 (2022).
22. K. Kawamura *et al.*, State dependence of climatic instability over the past 720,000 years from Antarctic ice cores and climate modeling. *Sci. Adv.* **3**, e1600446 (2017).
23. C. Buizert, A. Schmittner, Southern Ocean control of glacial AMOC stability and Dansgaard-Oeschger interstadial duration. *Paleoceanography* **30**, 2015PA002795 (2015).
24. S. J. Johnsen *et al.*, Irregular glacial interstadials recorded in a new Greenland ice core. *Nature* **359**, 311–313 (1992).
25. E. Capron *et al.*, The anatomy of past abrupt warmings recorded in Greenland ice. *Nat. Commun.* **12**, 2106 (2021).
26. W. Dansgaard, Stable isotopes in precipitation. *Tellus* **16**, 436–468 (1964).
27. J. Jouzel *et al.*, Validity of the temperature reconstruction from water isotopes in ice cores. *J. Geophys. Res.* **102**, 26471–26487 (1997).
28. M. Werner, U. Mikolajewicz, M. Heimann, G. Hoffmann, Borehole versus isotope temperatures on Greenland: Seasonality does matter. *Geophys. Res. Lett.* **27**, 723–726 (2000).
29. C. Charles, D. Rind, J. Jouzel, R. Koster, R. Fairbanks, Glacial-interglacial changes in moisture sources for Greenland: Influences on the ice core record of climate. *Science* **263**, 508–511 (1994).
30. L. C. Sime, P. O. Hopcroft, R. H. Rhodes, Impact of abrupt sea ice loss on Greenland water isotopes during the last glacial period. *Proc. Natl. Acad. Sci. USA* **116**, 4099–4104 (2019), 10.1073/pnas.1807261116, 201807261.
31. J. P. Severinghaus, T. Sowers, E. J. Brook, R. B. Alley, M. L. Bender, Timing of abrupt climate change at the end of the Younger Dryas interval from thermally fractionated gases in polar ice. *Nature* **391**, 141–146 (1998).
32. C. Goujon, J. M. Barnola, C. Ritz, Modeling the densification of polar firn including heat diffusion: Application to close-off characteristics and gas isotopic fractionation for Antarctica and Greenland sites. *J. Geophys. Res.* **108**, 18 (2003).
33. C. Huber *et al.*, Isotope calibrated Greenland temperature record over Marine Isotope Stage 3 and its relation to CH(4). *Earth Planet. Sci. Lett.* **243**, 504–519 (2006).
34. C. Buizert *et al.*, Greenland temperature response to climate forcing during the last deglaciation. *Science* **345**, 1177–1180 (2014).
35. L. Merlivat, J. Jouzel, Global climatic interpretation of the deuterium-oxygen 18 relationship for precipitation. *J. Geophys. Res.* **84**, 5029–5033 (1979).
36. S. J. Johnsen, W. Dansgaard, J. W. C. White, The origin of Arctic precipitation under present and glacial conditions. *Tellus* **41B**, 452–468 (1989).
37. D. A. Meese *et al.*, The accumulation record from the GISP2 core as an indicator of climate change throughout the holocene. *Science* **266**, 1680–1682 (1994).
38. I. Seierstad *et al.*, Consistently dated records from the Greenland GRIP, GISP2 and NGRIP ice cores for the past 104 ka reveal regional millennial-scale isotope gradients with possible Heinrich Event imprint. *Quat. Sci. Rev.* **106**, 29–46 (2014).
39. P. Kindler *et al.*, Temperature reconstruction from 10 to 120 kyr b2k from the NGRIP ice core. *Clim. Past* **10**, 887–902 (2014).
40. M. Guillevic *et al.*, Spatial gradients of temperature, accumulation and delta18O-ice in Greenland over a series of Dansgaard-Oeschger events. *Clim. Past* **9**, 1029–1051 (2013).
41. K. C. Martin *et al.*, Bipolar impact and phasing of Heinrich-type climate variability. *Nature* **617**, 100–104 (2023).
42. V. Masson-Delmotte *et al.*, Grip deuterium excess reveals rapid and orbital-scale changes in Greenland moisture origin. *Science* **309**, 118–121 (2005).
43. A. Landais *et al.*, Ice core evidence for decoupling between midlatitude atmospheric water cycle and Greenland temperature during the last deglaciation. *Clim. Past* **14**, 1405–1415 (2018).
44. V. Gkinis *et al.*, A 120,000-year long climate record from a NW-Greenland deep ice core at ultra-high resolution. *Sci. Data* **8**, 141 (2021).
45. C. He *et al.*, Abrupt Heinrich Stadial 1 cooling missing in Greenland oxygen isotopes. *Sci. Adv.* **7**, eabh1007 (2021).
46. T. Obase, A. Abe-Ouchi, Abrupt Bølling-Allerød warming simulated under gradual forcing of the last deglaciation. *Geophys. Res. Lett.* **46**, 11397–11405 (2019).
47. S. O. Rasmussen *et al.*, A first chronology for the North Greenland Eemian Ice Drilling (NEEM) ice core. *Clim. Past* **9**, 2713–2730 (2013).
48. J. Fohlmeister *et al.*, Global reorganization of atmospheric circulation during Dansgaard-Oeschger cycles. *Proc. Natl. Acad. Sci. U.S.A.* **120**, e2302283120 (2023).
49. P. Ciais, J. Jouzel, Deuterium and oxygen 18 in precipitation: Isotopic model, including mixed cloud processes. *J. Geophys. Res.* **99**, 16793–16803 (1994).
50. T. M. Dokken, K. H. Nisancioglu, C. Li, D. S. Battisti, C. Kissel, Dansgaard-Oeschger cycles: Interactions between ocean and sea ice intrinsic to the Nordic seas. *Paleoceanography* **28**, 491–502 (2013).
51. U. Hoff, T. L. Rasmussen, R. Stein, M. M. Ezat, K. Fahl, Sea ice and millennial-scale climate variability in the Nordic seas 90[thinsp]kyr ago to present. *Nat. Commun.* **7**, 12247 (2016).
52. T. L. Rasmussen, E. Thomsen, T. Nielsen, Water mass exchange between the Nordic seas and the Arctic Ocean on millennial timescale during MIS 4–MIS 2. *Geochem. Geophys. Geosyst.* **15**, 530–544 (2014).
53. G. H. Denton, R. B. Alley, G. C. Comer, W. S. Broecker, The role of seasonality in abrupt climate change. *Quat. Sci. Rev.* **24**, 1159–1182 (2005).
54. C. Buizert *et al.*, Greenland-wide seasonal temperatures during the last deglaciation. *Geophys. Res. Lett.* **45**, 1905–1914 (2018).
55. N. Siler *et al.*, The large-scale, long-term coupling of temperature, hydrology, and water isotopes. *J. Clim.* **34**, 6725–6742 (2021).
56. B. R. Markle, E. J. Steig, Improving temperature reconstructions from ice-core water-isotope records. *Clim. Past* **18**, 1321–1368 (2022).
57. S. R. Hemming, Heinrich events: Massive late pleistocene detritus layers of the North Atlantic and their global climate imprint. *Rev. Geophys.* **42**, RG1005 (2004).
58. W. Dansgaard *et al.*, A new Greenland deep ice core. *Science* **218**, 1273–1277 (1982).
59. C. U. Hammer *et al.* "Continuous impurity analysis along the dye 3 deep core" in *Greenland Ice Core: Geophysics, Geochemistry, and the Environment.* (1985), https://doi.org/10.1029/GM033p0090, pp. 90–94.
60. N. S. Gundestrup, B. L. Hansen, Bore-Hole Survey at Dye 3, South Greenland. *J. Glaciol.* **30**, 282–288 (1984).
61. B. M. Vinther *et al.*, Holocene thinning of the Greenland ice sheet. *Nature* **461**, 385–388 (2009).
62. I. M. Whillans, K. C. Jezek, Folding in the Greenland Ice Sheet. *J. Geophys. Res. Solid Earth* **92**, 485–493 (1987).
63. E. D. Waddington, J. F. Bolzan, R. B. Alley, Potential for stratigraphic folding near ice-sheet centers. *J. Glaciol.* **47**, 639–648 (2001).
64. M. F. Simonsen *et al.*, East Greenland ice core dust record reveals timing of Greenland ice sheet advance and retreat. *Nat. Commun.* **10**, 4494 (2019).
65. C. Stowasser *et al.*, Continuous measurements of methane mixing ratios from ice cores. *Atmos. Meas. Tech.* **5**, 999–1013 (2012).
66. J. Liisberg, *Abrupt Climate Change and the Nitrogen Cycle* (University of Copenhagen, Copenhagen, Denmark), 2020), p. 163.
67. T. Sowers, Dye 3 trapped gas isotopic analyses covering abrupt warming episodes during last glacial period. Arctic Data Center. https://doi.org/10.18739/A21N7XN9Q. Deposited 10 March 2022.
68. T. Sowers, Elemental and isotopic composition of oxygen (O2) and nitrogen (N2) in the Renland Ice Cap (RECAP) ice core. Arctic Data Center. https://doi.org/10.18739/A2C824F12. Deposited 7 December 2018.
69. V. Gkinis *et al.*, An ultra-high resolution water isotope record (d18O, dD) from the Renland ice cap spanning 120,000 years of climate history. PANGAEA, https://doi.org/10.1594/PANGAEA.966693. Deposited 6 February 2024.
70. T. R. Jones *et al.*, Improved methodologies for continuous-flow analysis of stable water isotopes in ice cores. *Atmos. Meas. Tech.* **10**, 617–632 (2017).
71. P. M. Grootes, M. Stuiver, J. W. C. White, S. Johnsen, J. Jouzel, Comparison of oxygen isotope records from the GISP2 and GRIP Greenland ice cores. *Nature* **366**, 552–554 (1993).
72. NGRIP-Project-Members, High-resolution record of Northern Hemisphere climate extending into the last interglacial period. *Nature* **431**, 147–151 (2004).
73. I. Oyabu *et al.*, The Dome Fuji ice core DF2021 chronology (0–207 kyr BP). *Quat. Sci. Rev.* **294**, 107754 (2022).
74. C. Buizert *et al.*, Antarctic surface temperature and elevation during the Last Glacial Maximum. *Science* **372**, 1097–1101 (2021).
75. M. M. Herron, C. C. Langway, Firn densification: An empirical model. *J. Glaciol.* **25**, 373–385 (1980).
76. J. Schwander *et al.*, Age scale of the air in the summit ice: Implication for glacial-interglacial temperature change. *J. Geophys. Res.* **102**, 19483–19493 (1997).
77. C. Buizert, DynaDens. GitHub. https://github.com/ChristoBuizert/DynaDens. Deposited 3 June 2024.
78. J. Lohmann, P. D. Ditlevsen, Objective extraction and analysis of statistical features of Dansgaard-Oeschger events. *Clim. Past* **15**, 1771–1792 (2019).
79. B. Bereiter *et al.*, Revision of the EPICA Dome C CO2 record from 800 to 600 kyr before present. *Geophys. Res. Lett.* **42**, 2014GL061957 (2015).
80. L. E. Lisiecki, M. E. Raymo, A Pliocene-Pleistocene stack of 57 globally distributed benthic δ18O records. *Paleoceanography* **20**, PA1003 (2005).
81. A. Berger, M.-F. Loutre, Insolation values for the climate of the last 10 million years. *Quat. Sci. Rev.* **10**, 297–317 (1991).
82. C. Buizert *et al.*, The Greenland spatial fingerprint of Dansgaard-Oeschger events in observations and models. Arctic Data Center. https://doi.org/10.18739/A2V698D8Z. Deposited 9 April 2024.
83. M. D. Holloway, L. C. Sime, J. S. Singarayer, J. C. Tindall, P. J. Valdes, Reconstructing paleosalinity from δ18O: Coupled model simulations of the Last Glacial Maximum, Last Interglacial and Late Holocene. *Quat. Sci. Rev.* **131**, 350–364 (2016).
84. J. Nusbaumer, T. E. Wong, C. Bardeen, D. Noone, Evaluating hydrological processes in the Community Atmosphere Model Version 5 (CAM5) using stable isotope ratios of water. *J. Adv. Modeling Earth Systems* **9**, 949–977 (2017).
85. E. Brady *et al.*, The connected isotopic water cycle in the community earth system model version 1. *J. Adv. Modeling Earth Syst.* **11**, 2547–2566 (2019).
86. C. Risi, S. Bony, F. Vimeux, J. Jouzel, Water-stable isotopes in the LMDZ4 general circulation model: Model evaluation for present-day and past climates and applications to climatic interpretations of tropical isotopic records. *J. Geophys. Res.* **115**, D12118 (2010).
87. M. Werner *et al.*, Glacial–interglacial changes in H218O, HDO and deuterium excess – results from the fully coupled ECHAM5/MPI-OM Earth system model. *Geosci. Model Dev.* **9**, 647–670 (2016).
88. J.-E. Lee, I. Fung, D. J. DePaolo, B. Otto-Bliesner, Water isotopes during the Last Glacial Maximum: New general circulation model calculations. *J. Geophys. Res.* **113**, D19109 (2008).
89. G. Hoffmann, J. Jouzel, V. Masson, Stable water isotopes in atmospheric general circulation models. *Hydrol. Processes* **14**, 1385–1406 (2000).
90. National Center for Atmospheric Research, iTRACE: An isotope-enabled Transient Climate Experiment for the last deglaciation. https://www.cesm.ucar.edu/working-groups/paleo/simulations/cesm1-itrace. Deposited 1 April 2021.
91. J. W. Hurrell *et al.*, The community earth system model: A framework for collaborative research. *Bull. Am. Meteorol. Soc.* **94**, 1339–1360 (2013).
92. J. Hu, J. Emile-Geay, J. Nusbaumer, D. Noone, Impact of convective activity on precipitation δ18O in isotope-enabled general circulation models. *J. Geophys. Res.* **123**, 13595–13610 (2018).
93. C. Li, D. S. Battisti, D. P. Schrag, E. Tziperman, Abrupt climate shifts in Greenland due to displacements of the sea ice edge. *Geophys. Res. Lett.* **32**, L19702 (2005).
94. M. Kageyama *et al.*, The PMIP4 contribution to CMIP6-Part 4: Scientific objectives and experimental design of the PMIP4-CMIP6 Last Glacial Maximum experiments and PMIP4 sensitivity experiments. *Geosci. Model Dev.* **10**, 4035–4055 (2017).